ACS APPLIED MATERIALS & INTERFACES

www.acsami.org

Research Article

Airbag-like Comb Flexible Pressure Sensor and Its Wearable Applications

Yingxi Xie, Sheng Bian, Longsheng Lu, Hanxian Chen, Jiayue Liao, Yuxuan Liang, and Xiaohua Wu*

Cite This: ACS Appl. Mater. Interfaces 2025, 17, 34230−34240

Read Online

ACCESS | Metrics & More | Article Recommendations | Supporting Information

ABSTRACT: Flexible wearable devices demonstrate immense potential in healthcare and human−computer interaction, yet the development of high-performance flexible pressure sensors for these applications remains a pressing technical challenge. Inspired by the structure of commonly used airbag combs, an airbag-like comb flexible pressure sensor (ALCS) was designed and fabricated using laser direct writing (LDW) technology. By incorporating an airbag structure to enhance the variation in contact area between the sensing and electrode layers, coupled with pore design to further boost unit strain, the ALCS achieved an ultrawide detection range (1.27−2783.815 kPa), high sensitivity (up to 21.53 kPa^{-1}), and exceptionally fast response/recovery times (3.4 ms/34 ms). To tackle the issue of lacking dynamic sign language recognition systems, we fabricated an intelligent glove (ALCIG) based on ALCS, which, when integrated with machine learning algorithms, achieved precise recognition of 8 types of dynamic sign language, offering an efficient solution for barrier-free communication for individuals with speech impairments. To further evaluate the recognition capabilities of ALCIG and enhance its applicability in diverse scenarios, we developed a virtual keyboard letter recognition test involving 26 categories. The results demonstrated that even with 26 highly complex targets, ALCIG successfully collected data and achieved accurate classification, showcasing its significant potential in gesture recognition and complex classification tasks.

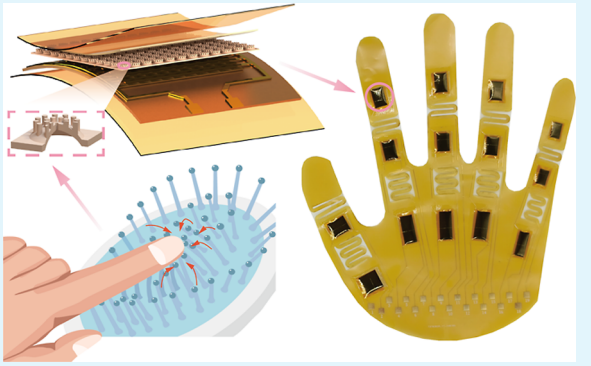

KEYWORDS: *flexible pressure sensor, airbag-like comb structure, gesture recognition, machine learning, intelligent glove*

1. INTRODUCTION

With the rapid advancements in flexible electronics and artificial Internet of Things (IoT) technologies, flexible wearable devices are demonstrating extensive application potential in fields like vital sign monitoring,[1−3] medical health rehabilitation,[4,5] human−machine interaction,[6−9] and gesture recognition.[10−12] In these devices, high-performance flexible pressure sensors serve as critical components capable of detecting various pressure changes with greater speed and accuracy. Flexible pressure sensors can be categorized into four types based on their working mechanisms: capacitive,[13−15] piezoelectric,[16,17] piezoresistive,[18,19] and triboelectric.[20,21] And piezoresistive sensors are extensively employed due to their advantages, including a wide pressure detection range, simple detection methods, and low power consumption.

To enhance the sensitivity, detection range, stability, and other performance metrics of sensors, researchers commonly adopt various strategies. One approach is to utilize various advanced materials for the sensing layer, such as MXene,[22−24] carbon nanotubes,[25] graphene,[26−28] metal nanowires,[29,30] and conductive polymers like polypyrrole (PPy),[31,32] which exhibit excellent conductivity, high mechanical strength, and stable electrical connections during both loading and unloading. The second approach involves microstructural fabrication of the sensing or substrate materials to achieve specific microstructural forms, such as microspherical,[13,33,34] micropillar,[12,35,36] and micropyramid shapes,[37,38] etc. Some researchers have designed layered or hierarchical microstructures to achieve improved stress distribution.For example, Yang et al.[39] ingeniously fabricated a biomimetic micro dome structure by replicating and transferring the microstructure of rose petals, and developed a biomimetic flexible piezoresistive sensor with a layered microstructure, successfully improving the sensitivity of the sensor. Du et al.[40] fabricated a flexible pressure sensor with a two-tier microstructure by combining silver nanowire coatings and laser ablation, When the sensor is under pressure, the deformation of the first-order microstructure increases the contact area between the two functional layers. When the first-order microstructure becomes difficult to deform, the second-order microstructure contacts the interdigital electrode, and the resistance of the sensor always

Received: March 14, 2025
Revised: May 26, 2025
Accepted: May 27, 2025
Published: June 2, 2025

https://doi.org/10.1021/acsami.5c05118
ACS Appl. Mater. Interfaces 2025, 17, 34230−34240

maintains a linear decrease. Under identical pressure, these microstructures show more concentrated contact stress and strain, resulting in more significant compressive deformation and improved compressibility. One frequently used method for fabricating the desired microstructures involves lithography. This process first creates an inverse pattern on materials like silicon or copper and then coats the substrate material, such as polydimethylsiloxane (PDMS),[41,42] onto the prepared mold to achieve the desired micropattern. However, the conventional lithography process is time-consuming and costly, particularly when dealing with more complex 3D structures, making fabrication more challenging. Furthermore, the inefficiency stemming from the need for frequent modifications to initial designs and the repeated fabrication of prototypes is a considerable drawback of this technique.[43] Additionally, the replication process, which involves PDMS coating, curing, demolding, and assembly, presents significant challenges and may lead to a decrease in the consistency of the final structural quality. While 3D printing is capable of fabricating more complex structures, its precision for small structures is limited, and the surface quality is often poor, making it difficult to achieve the intended results.[44] In contrast, laser direct writing (LDW) technology, due to its high precision, low processing costs, strong consistency, and excellent controllability, can accurately fabricate the desired results under the premise of a defined processing pattern. Table S1 shows the comparison between LDW and lithography and 3D printing. LDW has advantages in cost and processing time. The advantage of lithography is that the processing resolution can be smaller, while the main advantage of 3D printing is lower cost.[45,46] Additionally, LDW technology offers the ability to conveniently alter the microstructure morphology by adjusting laser parameters, providing a distinct advantage in the fabrication of small structures and even multitiered architectures. For instance, Zhang et al.[47] used laser direct writing to fabricate a flexible piezoresistive sensor with curved conical microstructures, with an initial sensitivity of 21.80% kPa^{-1} and a detection range exceeding 20 kPa. Zhang et al.[48] employed laser technology to create a highly ordered piezoresistive sensor with a two-level microstructure. The two-level microstructure, with its higher flexibility and increased contact points, demonstrated 20 times the sensitivity of the single-level microstructure sensor. Although there are various microstructure designs for flexible pressure sensors, most designs focus only on single-sided microstructures, neglecting the significant potential of double-sided microstructures in enhancing sensor performance. And at least one side of the current double-sided sensor has an irregular microstructure. For example, Xiao et al.[49] applied the polymer mixture on the prepared sandpaper and then covered the top surface of the ion gel with another sandpaper to obtain a iontronic dielectric layer. Yuan et al.[50] prepared the dielectric layer with one side of regular micropyramid shape and the other side of irregular protrusion shape by using silicon substrate and abrasive paper. Fewer sensors with regular microstructure on both sides. Additionally, current gesture recognition primarily focuses on static gestures, such as simple "OK" or "1" signs, while dynamic sign language recognition remains a significant challenge.

In this study, inspired by the commonly used airbag comb, an airbag-like comb flexible pressure sensor was designed and fabricated using laser direct writing technology. Due to its backside airbag and pore microstructure, the sensor exhibits high sensitivity (up to 21.53 kPa^{-1}), an ultrawide operating range (1.27−2783.815 kPa), and ultrafast response/recovery times (3.4 ms/34 ms). To demonstrate its potential applications, the sensor was used to detect human physiological activity signals, such as head movements and muscle pressure. Moreover, we fabricated an intelligent glove using this sensor, and by integrating machine learning algorithms, the glove effectively collects data for recognizing 8 dynamic sign language gestures and 26 virtual keyboard letter inputs. The glove achieves classification accuracies of 98.86% and 98.01%, respectively, highlighting its immense application potential in gesture recognition and various complex recognition tasks.

2. EXPERIMENTAL SECTION

2.1. Materials for sensor and Glove. The sensing layer material of the sensor is graphite nickel plated silica gel (HSD-16715, Dongguan Shunyi Plastic Materials Co., Ltd.). The isolation layer material is polyimide (Dongguan Ronghui Insulation Materials Co., Ltd., thickness: 125 μm). The electrode layer material is copper (Shenzhen JLC Technology Group Co., Ltd.). The top encapsulation layer material is medical polyurethane (PU, Cofoe Medical Equipment Co., Ltd., thickness: 100 μm). The bottom encapsulation layer material is polyimide (Shenzhen JLC Technology Group Co., Ltd.). The materials of each layer of gloves and the corresponding layers of sensors are consistent.

2.2. Manufacturing Parameters of ALCS Sensing Layer. The sensing layer was subjected to surface microstructural treatment using laser direct writing technology, which was divided into four parts: backside processing, front processing, front perforation, and front trimming. The laser processing images of the back and front processing are shown in Figure S1, and the single processing image of the front perforation is a circle with a diameter of 120 μm. The complete machining diagram is a 12 × 12 array of a single machining diagram, with a spacing of 18/11 mm between each row and column. Due to the need to be processed into an airbag-like shape, the concentric circle structure on the back is denser inward, while the concentric circle structure on the front is sparser inward. The diameter of the micro column reserved on the front is 160 μm. Initially, the conductive silicone was cut into 20 mm−20 mm pieces using an ultraviolet laser with default laser parameters (frequency: 30 kHz, processing speed: 200 mm/s, current: 1 A, on-delay: 300 μs, off-delay: 100 μs, end-delay: 300 μs, corner-delay: 100 μs, spot size: 0.001 mm, wavelength: 355 nm). The surface was subsequently cleaned with ethanol and deionized water before being dried. The airbag structure on the backside of the sensing layer was processed first, with 6 iterations, laser frequency set to 30 kHz, processing speed at 200 mm/s, processing current of 1 A, and all delay parameters (on, off, end, and corner) set to 0, to prevent excessive uncut areas. The front structure of the sensing layer was then processed, with 7 iterations, laser frequency at 30 kHz, processing speed of 200 mm/s, processing current of 1 A, on-delay set to 200 μs, off-delay to 0, end-delay to 300 μs, and cornerdelay to 0, to avoid uneven heights in the structure. The pore structure of the sensing layer was then processed, requiring 35 times to perforate the entire sensing layer, with default laser parameters. Lastly, the front of the sensing layer was cut to expose the front structure, using the fill function in the laser software with a line spacing of 0.012 mm and 3 iterations, with default laser parameters. After completing the four processing steps, the resulting sensing layer exhibited a 12 × 12 micro airbag comb structure. Due to the residual clumped carbonized layer left by the laser processing, medical cotton swabs soaked in anhydrous ethanol were used to clean both sides of the sensing layer to remove the carbonized layer.

2.3. Performance Measurements and Characterization. The microstructure of the sensing layer is processed using ultraviolet lasers (HT-M5UV, Zhongshan Hantong Laser Equipment Co., Ltd.). The final morphology of the sensing layer was observed by field emission scanning electron microscopy (FE-SEM, Carl Zeiss). Obtain the 3D contour plot of the sensing layer after processing using a 3D contour measuring instrument (Keyence (China) Co., Ltd.). A stable external

https://doi.org/10.1021/acsami.5c05118
ACS Appl. Mater. Interfaces 2025, 17, 34230−34240

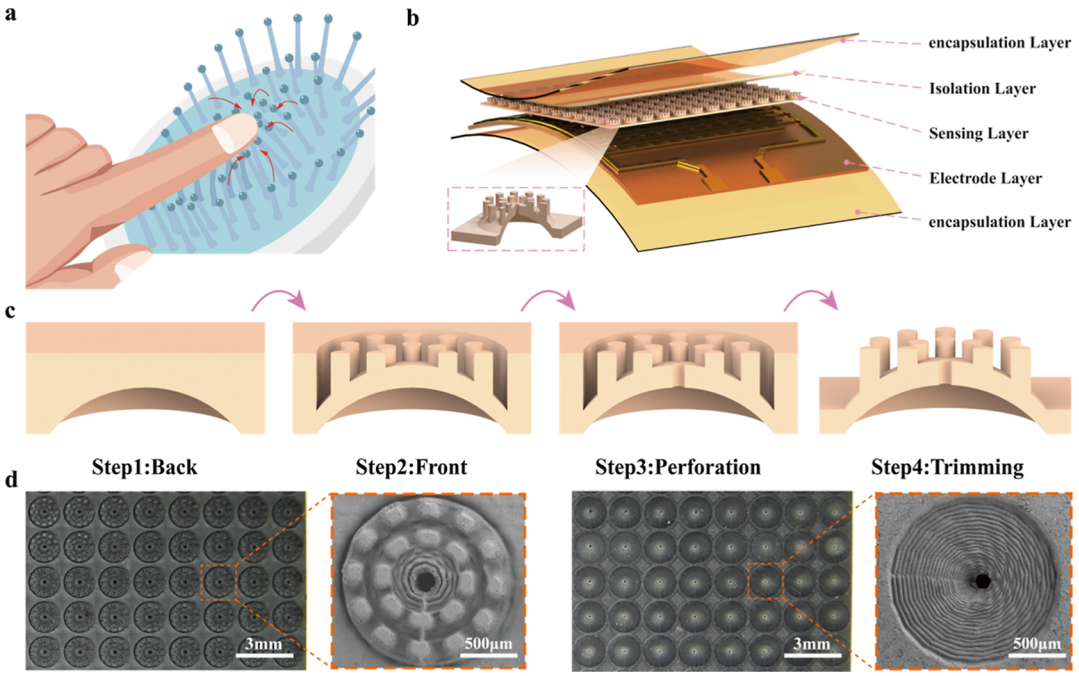

Figure 1. Inspiration and fabrication process. (a) Example of force-induced deformation in the airbag comb structure. (b) Assembly process of the ALCS. (c) Fabrication process of the ALCS sensing layer. (d) Scanning electron microscope images of the front and back sides of the ALCS sensing layer.

pressure was applied on the pressure sensor with a static testing machine (3344L39272kN, Instron). A digital multimeter (2400A, Keithley) was used to real-time record the electrical signals in the dynamic compression/relaxation process.

3. RESULTS AND DISCUSSION

3.1. Design and Fabrication of an Airbag-Like Comb Flexible Pressure Sensor. The airbag comb is a commonly used daily item, and in contrast to a flat comb, it incorporates an airbag in the comb's base, as depicted in Figure 1a. When pressure is applied, it can be observed that the comb teeth move toward the pressed surface. The soft base design allows it to respond to even small pressures by converging, while the perforations on the comb balance the pressure difference between the inside and outside of the airbag, preventing pressure saturation under high pressure and maximizing the convergence effect. To simulate this phenomenon, an airbag-like comb flexible pressure sensor (ALCS) has been designed. When pressure is applied, the ALCS not only demonstrates deformation of the microstructure but also exhibits the convergence of the microstructure toward localized pressure, allowing for a more sensitive response output to localized pressure. Figure 1b shows the overall assembly process of the ALCS, which consists of an isolation layer, sensing layer, electrode layer, and top and bottom encapsulation layers. The purpose of the isolation layer is to isolate the sensing layer from the top encapsulation layer, preventing the microstructure of the sensor from being in direct contact with the encapsulation layer under pressure, which could prevent the microstructure from returning to its original state. The sensing layer converts mechanical input signals into measurable electrical signals, and transmits them via the electrode layer. The electrode layer uses interdigitated electrodes as conductive paths, and is laminated on the bottom encapsulation layer by high temperature. One side of the top encapsulation layer contains pressure sensitive adhesive. After each layer is placed in the manner shown in Figure 1b, the entire sensor is encapsulated by bonding the top encapsulation layer and the bottom encapsulation layer. Figure 1c shows the detailed fabrication process of the ALCS sensing layer, where laser direct writing technology is used to create surface microstructures on the conductive silicone, divided into four steps: backside processing, front-side processing, front-side perforation, and front-side trimming. The backside processing is used to fabricate the airbag structure, the front-side processing is used for the micropillar structure, the front-side perforation is for creating the holes in the middle, and the front-side trimming removes excess parts from the microstructures to expose the frontside microstructure. Figure 1d presents the scanning electron microscope (SEM) image of the ALCS sensing layer. After processing, the ALCS sensing layer may have residual clumped carbonized material above the micropillars, likely caused by the vaporization of the cut portions during the laser processing, which then deposit on the tops of the unprocessed higher micropillars, forming irregular clumped structures. The presence of this carbonized material can affect the deformation stability of the ALCS under pressure, leading to the detection of different response signals when the same pressure is applied. To avoid this issue, the ALCS sensing layer requires surface cleaning after processing. Ultrasonic treatment was performed on the sensing layer with 99.7% ethanol and deionized water for 5 min each, and then placed in a constant temperature oven to dry at 50 °C for 10 min. After cleaning, the tops of the micropillars exhibit a dense, scaly structure, enabling uniform deformation of the micropillars under pressure, thereby improving the stability of the ALCS. The comparison diagram of the ALCS sensing layer before and after cleaning is shown in Figure S2. After cleaning, the micropillar surface reveals a dense, scale-like structure, allowing for stable deformation under pressure. Additionally, the backside structure has a dual-layer microstructure, which

https://doi.org/10.1021/acsami.5c05118
ACS Appl. Mater. Interfaces 2025, 17, 34230−34240

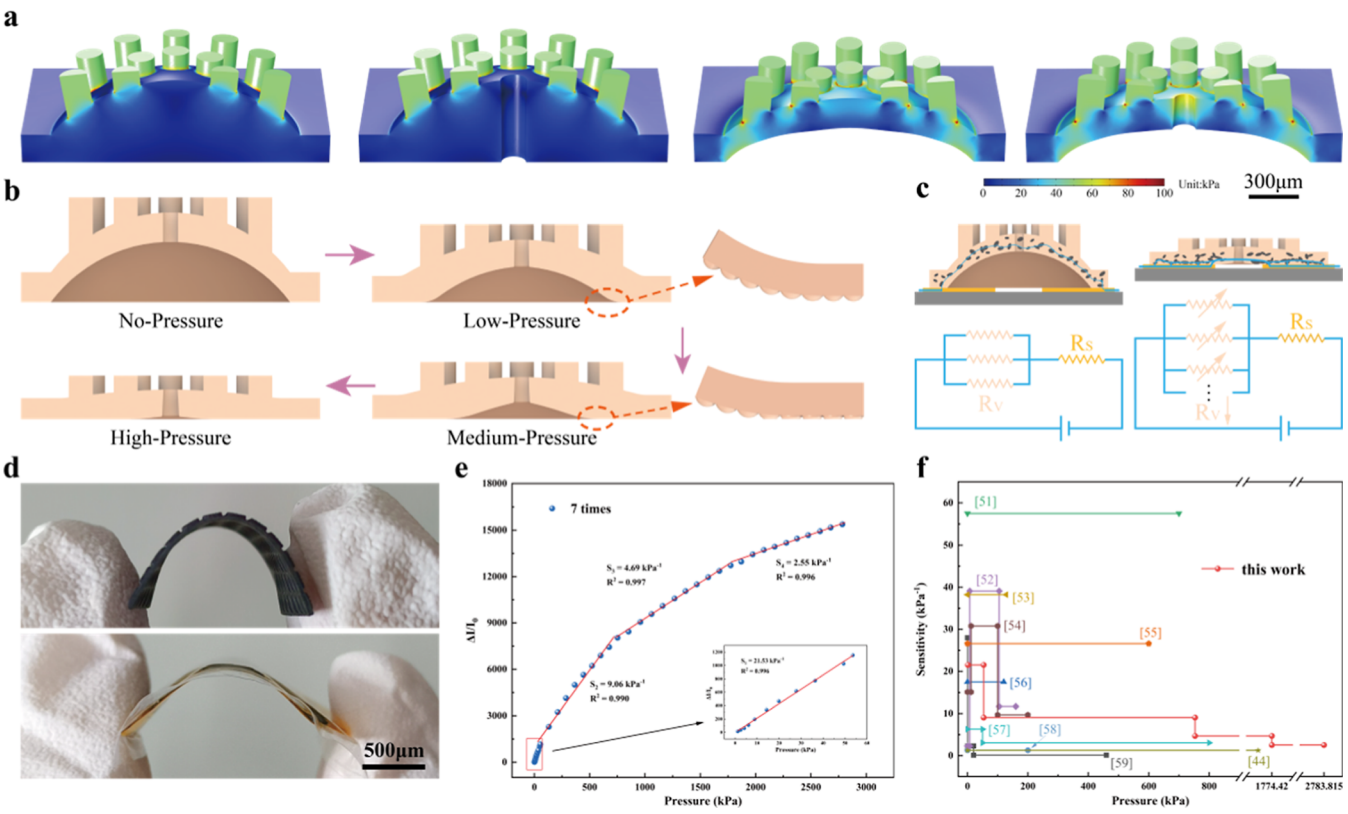

Figure 2. Structural characteristics of ALCS. (a) Comparative analysis of four simulations examining the role of the back airbag and pore structures. (b) Deformation behavior of the ALCS sensing layer under varying pressure conditions. (c) Schematic of the pressure sensing mechanism of ALCS. (d) Real image of ALCS and its sensing layer under bending. (e) Sensitivity and response range of ALCS under optimal fabrication conditions. (f) Performance comparison between ALCS and reported microstructured pressure sensors.

significantly enhances the sensor's response range and sensitivity.

3.2. Structural Characteristics of ALCS. As shown in Figure 2a, under identical initial conditions, a comparison of four microstructures with and without backside airbag and perforation structures reveals that the airbag-like comb structure, processed with both backside airbag and perforation structures, demonstrates the highest force sensitivity. Compared with traditional micropillar-dome coupled force-sensitive structures, the introduction of the airbag changes the deformation direction of the traditional micronano structure, causing the deformation of the microcolumns to converge toward the pressure direction rather than diverge, significantly increasing the change in contact area with increasing pressure. The introduction of pore ensures further improvement of unit strain, and increasing the pore helps avoid the rapid rise in air pressure under high pressure, ensuring the continued deformation of the airbag-like comb structure under high pressure. Furthermore, the pore can optimize the lateral deformation path of the substrate after longitudinal compression. The relevant simulation parameters are provided in Table S2. Simulations comparing commonly used microstructures (such as micropyramids, microcolumns, and microspheres) were also performed, and the relevant simulation results are shown in Figure S3. A simulation comparison between ALCS and three common microstructures is performed (with the microspherical structure shown only halfway for clarity), using parameters consistent with Table S2. The stress in the micropyramid structure is concentrated at the upper part of the pyramid, failing to efficiently transfer stress to the lower section. Although the micropillars structure experiences larger stresses on each pillar, with stress concentration at the pillar-bottom contact, the lack of a backside airbag structure prevents significant deformation at the bottom. The stress in the microspherical structure is primarily concentrated below the edges of the sphere, resulting in the least deformation under the same pressure. The ALCS combining the stress transfer of micropillars with the deformability of the back airbag, demonstrates the largest deformation and the most concentrated stress among the four microstructures. Figure 2b illustrates the deformation behavior of the ALCS sensing layer under varying pressure conditions. At the initial stage, the contact area between the back of the sensing layer and the electrode layer is small, with sparse conductive paths. Furthermore, the distance between the conductive particles (primarily carbon black) inside the sensing layer is large, leading to higher resistance. As the pressure applied to the sensing layer increases, the structure is compressed first, which reduces the distance between the conductive particles and results in a decrease in the resistance of the sensing layer. As the pressure continues to increase, the contact area between the back of the sensing layer and the electrode layer gradually increases, and the number of conductive pathways increases, resulting in further decrease in the resistance of the sensing layer. It can also be observed that under relatively low pressure, the first protruding part of the two-layer microstructure on the back makes initial contact with the electrode layer. With the continued increase in pressure, the recessed layer between the two protruding parts gradually contacts the electrode layer, thus enlarging the contact area. Figure 2c shows the pressure

https://doi.org/10.1021/acsami.5c05118
ACS Appl. Mater. Interfaces 2025, 17, 34230−34240

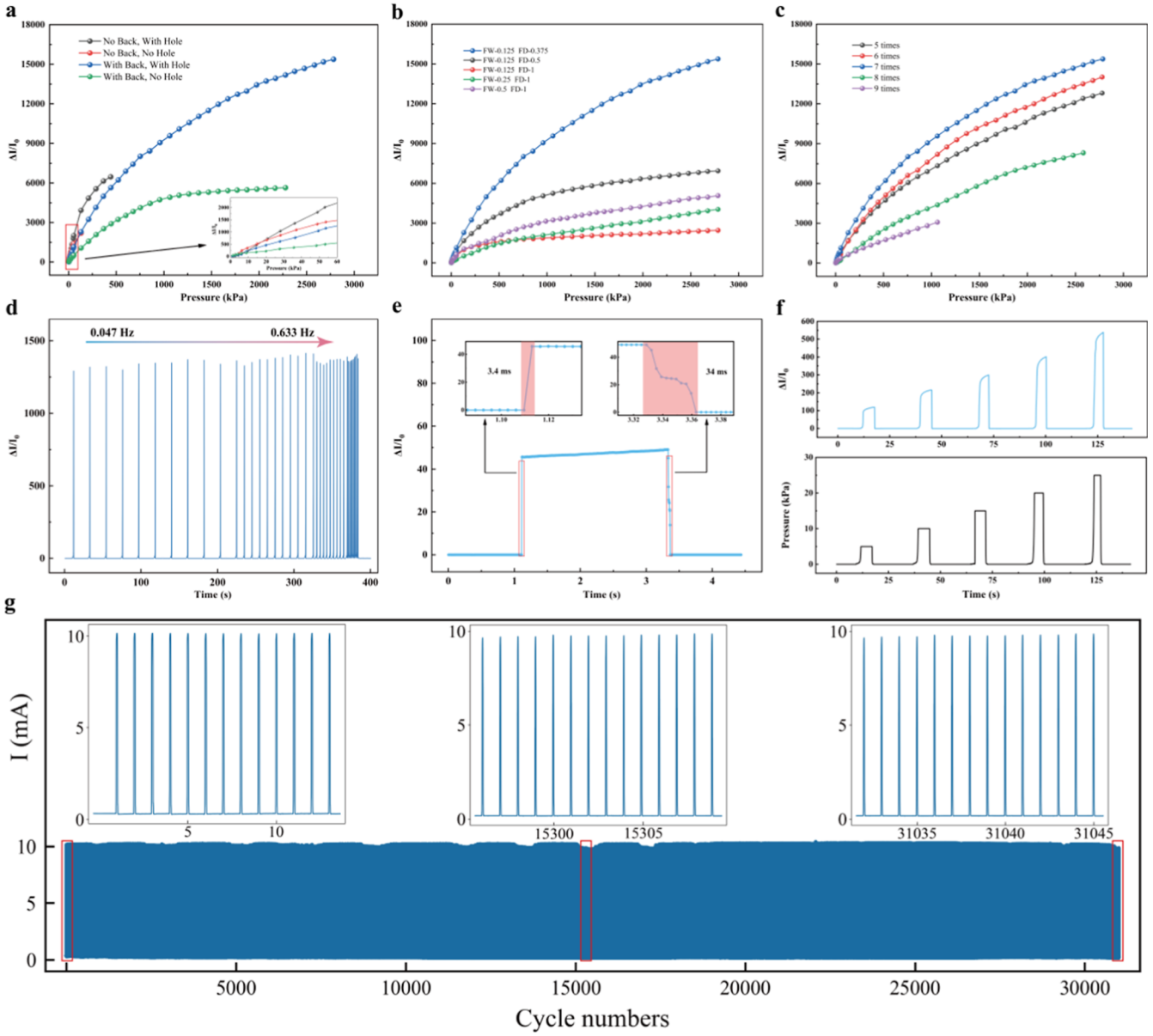

Figure 3. Sensor performance characteristics. (a) Comparison of sensor performance with different sensing layer structures. (b) Comparison of sensor performance with different finger parameters. (c) Comparison of sensor performance with different processing frequencies on the front of the sensing layer. (d) ALCS response under 50 kPa external force, with frequency ranging from 0.047 to 0.633 Hz. (e) Response and recovery time of ALCS under 3 kPa pressure. (f) Response of ALCS under different pressures. (g) Cyclic stability test of ALCS over 30,000 cycles.

sensing mechanism of ALCS, where R_V represents the resistance of the sensing layer and RS represents the resistance of the interdigital electrode, which can be treated as a constant. As pressure continues to rise, the resistance R_V gradually decreases, while the contact area between the back of the sensing layer and the electrode layer increases, leading to an increase in the number of conductive pathways, thus further lowering the total resistance of the sensing layer. ALCS and its sensing layer demonstrate remarkable deformability. Figure 2d illustrates the deformation of ALCS and its sensing layer under a small force applied between two fingers, confirming its ability to adapt to the surface of the object being measured in various applications, making it suitable for environments where the measured object is likely to undergo deformation. Figure S4 shows the contact angle of the sensing layer and the ALCS, and it can be found that the sensing layer has excellent hydrophobicity due to the microstructural treatment of its surface, and the contact angle can reach 152.02°. While the surface material of ALCS is PU, its hydrophobicity is ordinary, and the contact angle is 80.66°. However, PU membrane has excellent waterproof property, which can ensure that water will not penetrate into the sensor. Figure 2e shows the sensitivity and response range of ALCS under optimal processing conditions, The sensitivity is defined as

$$S = (\Delta I/I_0)/P$$

where I_0 represents the current of ALCS in its initial state, ΔI is the difference between the current measured under pressure and the initial current, and P represents the pressure applied to ALCS. Under the optimal processing conditions, the sensor achieves a maximum sensitivity of 21.53 kPa^{-1} within an ultrawide pressure range of 1.27−2783.815 kPa. As shown in

https://doi.org/10.1021/acsami.5c05118
ACS Appl. Mater. Interfaces 2025, 17, 34230−34240

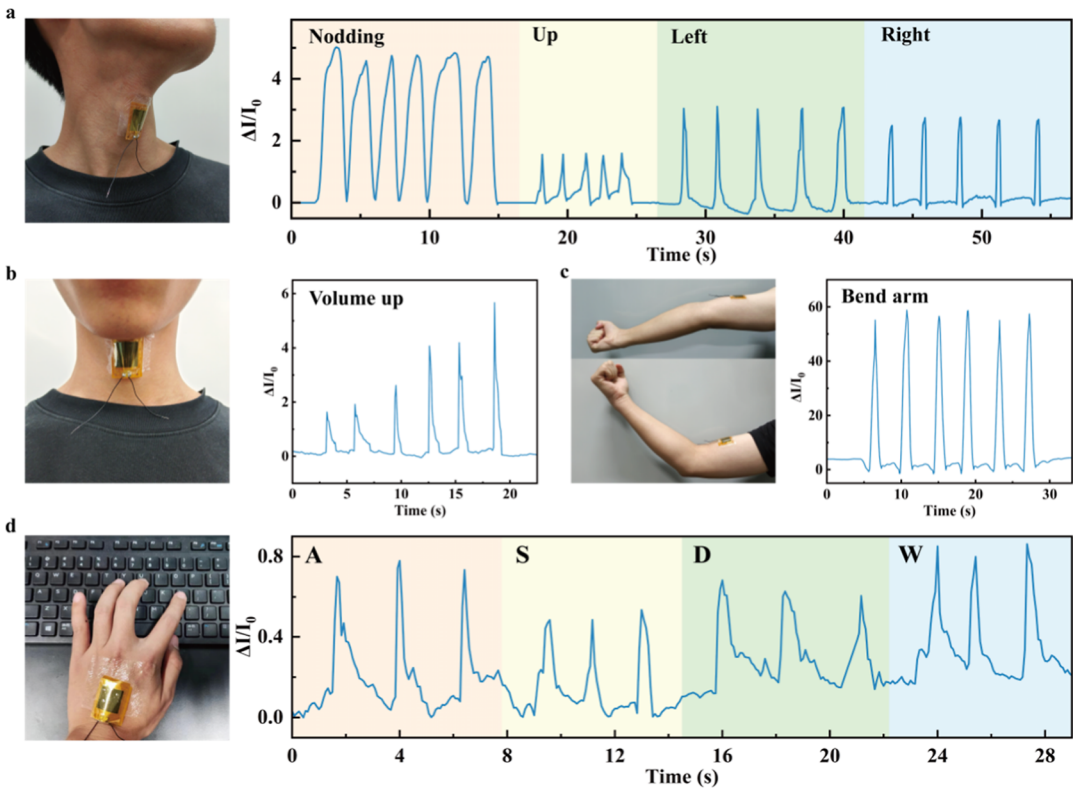

Figure 4. Basic application detection of ALCS: (a) detection of four types of head movements in the subject; (b) detection of variations in the subject's pronunciation of the same sound at different pitches; (c) detection of muscle pressure changes during the subject's arm flexion; (d) investigation of the signal variations when the subject types different letters on a keyboard.

Figure 2f, a performance comparison with reported microstructured flexible pressure sensors reveals that while some sensors demonstrate higher sensitivity than ALCS, their response range is significantly constrained.[44,51−59] By comparison, ALCS exhibits distinct advantages in terms of high sensitivity, ultrawide operating range and cycle numbers. For further details on the performance comparison, please refer to Table S3.

3.3. The Sensing Performance of ALCS. To further validate the performance of the four sensors with different microstructures shown in Figure 2a and 3a compares the sensing characteristics of these microstructured sensors. The results indicate that the sensors with backside airbag and pore microstructures exhibit the highest performance, while the response range of sensors without backside airbag is limited, and the sensitivity of sensors without pore is restricted. This is attributed to the introduction of airbags increasing the change in contact area with increasing pressure, thereby extending the response range; meanwhile, the introduction of pore enhances the unit strain increment. Figure 3b compares the impact of different interdigital electrode parameters on sensor performance, where FW denotes the finger width and FD represents the spacing between two fingers, both in millimeters. The study indicates that sensors with a higher proportion of actual interdigital electrode area exhibit significantly enhanced sensitivity. This improvement is attributed to the larger effective contact area between the ALCS sensing layer and the electrode layer under the same pressure, effectively increasing the number of conductive pathways and improving sensor sensitivity. The lower sensitivity associated with the parameters represented by the purple curve, compared to the blue and black curves, might be due to the 1.5 mm diameter of a microstructure in the ALCS sensing layer. Under compression, a substantial portion of its area does not align with the interdigital regions, thereby limiting the formation of conductive circuits. Figure S5 shows the effect of processing different microcolumn diameters in the sensing layer on the response performance of ALCS. It can be observed that as the microcolumn diameter gradually decreases, the sensitivity of ALCS increases under low pressure. This is because the smaller the microcolumn diameter, the easier it is to compress under the same pressure. However, correspondingly, sensing layers with smaller microcolumn diameters lack compressible volume under higher pressure conditions, while sensing layers with larger microcolumn diameters are more difficult to compress under the same pressure. Therefore, sensing layers with smaller or larger microcolumn diameters will reduce the sensitivity of ALCS. Figure S6 shows the effect of different pore diameters in the sensing layer on the response performance of ALCS. It can be observed that as the pore diameter increases, the sensitivity of ALCS improves significantly. This is because the pores avoid the influence of air in the back of the sensing layer on the compression process. However, correspondingly, sensing layers with larger pore diameters are also more susceptible to damage under high pressure, thereby reducing the response range of ALCS. Figure 3c compares the performance of ALCS under varying laser processing frequencies of the front surface. The results reveal that sensors processed seven times exhibit optimal sensitivity and response range. This is attributed to the maximized height of microcolumns formed after seven cycles, which significantly enhances deformation effects under identical pressure conditions. However, exceeding seven processing cycles results in reduced sensitivity and response range, likely due to overprocessing causing penetration of the

https://doi.org/10.1021/acsami.5c05118
ACS Appl. Mater. Interfaces 2025, 17, 34230−34240

Figure 5. Recognition of complex tasks by ALCS. (a) Application scenario of sign language gesture recognition. (b) Physical image of ALCIG. (c) Collection of 8 sign language data sets and visualization of dimensionality reduction after feature extraction. (d) Confusion matrix of sign language gesture recognition results on the test set. (e) Collection of 26 keyboard letter input data sets and dimensionality reduction visualization after feature extraction. (f) Confusion matrix of keyboard letter input recognition results on the test set.

sensing layer and damage to certain microstructures. Under higher pressures, these damaged structures deteriorate further, impairing overall performance. Therefore, it is necessary to balance micropillar height and structural integrity to achieve optimal performance. The 3D contour plot of the sensing layer under different processing cycles is shown in Figure S7. From the 3D contour plot, it can be observed that as the number of processing steps increases, the processing depth (i.e., the height of the micropillars) also increases, which contributes to improved performance. However, it should be noted that with the increase in processing depth, there is a potential risk of penetrating through the sensing layer. Although after 8 processing steps, there was no penetration of the sensing layer, the structural layer between the front and back surfaces becomes very thin, making it susceptible to collapse and damage under higher pressures. After 9 processing steps, penetration is evident from the image, which further worsens the collapse damage under pressure. Figure 3d shows the response of ALCS under a 50 kPa pressure at different frequencies, demonstrating that ALCS can operate under varying frequency conditions. The slight fluctuations are due to variations in the actual pressure applied by the tensile testing machine when setting a fixed value. Figure 3e shows that ALCS demonstrates an ultrafast response time (3.4 ms) and recovery time (34 ms) under 3 kPa pressure, indicating its significant advantage in detecting rapidly changing values. Figure 3f shows the response of ALCS under varying pressures (5, 10, 15, 20, 25 kPa), exhibiting a strong correspondence, indicating that ALCS can distinguish different pressure levels, while also revealing the perfect conductive network between the sensing layer and electrode layer. Figure 3g shows the cyclic performance of ALCS after 31,000 cycles, while Figure S8 displays the initial/final 100 cycle responses. The cyclic stability test shows that it has excellent repeatability and long-term stability, and can withstand over 30,000 loading/unloading cycles.

https://doi.org/10.1021/acsami.5c05118
ACS Appl. Mater. Interfaces 2025, 17, 34230−34240

3.4. The Practical Application of ALCS. Due to the remarkable flexibility and deformability of ALCS, it can effectively conform to irregular surfaces, allowing it to be worn on the subject for exploring its potential applications in the healthcare domain. Figure 4a presents ALCS fixed at the subject's neck, effectively distinguishing four head movements: nodding, looking up, turning left, and turning right, with the curves corresponding to different physiological movements exhibiting clear characteristics. Figure 4b presents the curve measured by ALCS when the subject pronounces the sound "*P*" with increasing volume. The results indicate that as the volume increases, the slight vibrations in the subject's throat skin intensify, leading to an increase in the signal value measured by ALCS, thus proving its ability to effectively differentiate subtle pressure variations. Figure 4c illustrates ALCS fixed at the subject's upper arm, enabling the detection of muscle pressure during motion, thereby demonstrating its excellent stability and reliability in practical applications. Figure 4d presents the preliminary installation of ALCS on the back of the hand. The results demonstrate that ALCS can capture corresponding characteristic signals when different letters are input. The feature signals are expected to be accurately classified by machine learning, which provides a preliminary verification for virtual keyboard input recognition of wearable devices based on ALCS and proves its practical feasibility. To explore the application scenarios of ALCS under high pressure, it was fixed at the heel of the insole. Figure S9 shows the response changes of ALCS during subject's sitting, standing, and walking, proving that it can still distinguish different movement states of subject under high pressure and maintain stability in response changes. Considering that ALCS may be affected by oil stain, sand and dust in actual use scenarios, the practical feasibility of ALCS is studied. Simulate the impact of dust friction on ALCS by sanding the ALCS surface with 220 mesh abrasive paper for 30 s. Apply silicone oil to the ALCS surface to simulate the effect of oil contamination on the ALCS. Figure S10 shows the response curve of ALCS after friction and after oiling compared with the default case. It can be found that after friction and oiling, the response of ALCS can still maintain excellent consistency, proving its extraordinary practical feasibility.

The proposed ALCS is employed in the fabrication of a hand-shaped sensor array and the development of intelligent gloves, suitable for applications such as hand motion reconstruction, virtual keyboard input, and sign language recognition. Figure 5a depicts the practical application of sign language gesture recognition. Without knowledge of sign language, communication between a normal person and an individual with speech or hearing disabilities can be challenging. However, if the individual with disabilities wears an intelligent glove capable of recognizing sign language, the communication will be much smoother. Figure 5b shows the intelligent glove made using ALCS (ALCIG). The glove is designed with serpentine patterns at the joints to ensure that during large-movement sign language operations, the wearer can perform the desired actions without being restricted by the glove. The glove's electrode layer continues to use interdigitated electrodes, with the signals centralized for easy extraction from the bottom of the glove. The sensing layer structure between each finger joint is provided in Figure S11. Due to the differences in finger width, the number of microstructures in the sensing layer between each finger joint also varies. The relevant parameters are shown in Table S4. These sensing layers are obtained by adding an additional cutting step after the original processing steps to achieve the required structure. Here, the sensing layer structure between the joints of the right-hand is used as an example, and the sensing layer structure of the left-hand is a mirror image of that of the right-hand. To assess the effectiveness and accuracy of ALCS in extracting target information, we employed Convolutional Neural Networks (CNN) to analyze the signals and pattern recognition data collected by ALCS. The convolutional layers are responsible for feature extraction, while the fully connected layers combine and output the classification results, ensuring the complete decoding of sensor signals. The raw waveform plots of the various sign language gestures collected by ALCIG are provided in Figure S12. We employ the t-distributed Stochastic Neighbor Embedding (t-SNE) algorithm to project high-dimensional data into two dimensions. A total of 2561 data segments were collected as the training data set for sign language gesture recognition, and 701 data segments were used to test the accuracy of the model. The data collection video can be found in the Movie S1. The distribution of all data sets was obtained using t-SNE dimensionality reduction. The training parameters and evaluation of the associated deep learning models can be found in Table S5. As shown in Figure 5c, these eight dynamic signals are grouped into several clusters, which can be easily distinguished. The meaning represented by each gesture signal can be provided in Table S6. In the context of English communication, the sequence of these gestures expresses the following: Nice to meet you! What's your name? Thank you. Figure 5d shows the confusion matrix for the trained model on eight types of sign language gestures, with an accuracy of 98.86% on the test set. These results not only demonstrate the high quality of the different gesture data collected by ALCS but also indicate the potential application of the fabricated ALCIG in sign language gesture recognition.

To further validate whether ALCIG can effectively capture key features from more complex inputs and enhance its practicality across various application scenarios, we established a 26-class virtual keyboard letter recognition test, collecting 6511 data segments as the training data set and using 1360 data segments to test the model's accuracy. The results of the test and dimensionality reduction classification are shown in Figure 5e. Due to the high similarity in gestures between some of the 26 letters (e.g., the letters "a" and "z"), misclassification occurred in the test results. Figure 5f shows the typical confusion matrix for the 26 input letters, with an accuracy of 98.01% on the test set. This result demonstrates that even in detecting 26 classes with numerous targets, ALCIG successfully collects data and performs effective classification, validating its immense potential in gesture recognition.

4. CONCLUSIONS

Inspired by the commonly used airbag comb, an airbag-like comb flexible pressure sensor was designed and fabricated using laser direct writing technology. The introduction of the backside airbag and pore structures in the ALCS sensing layer increases the variation in the contact area between the sensing and electrode layers under pressure, while the pore structure ensures a further enhancement of the strain per unit. This structure enables the ALCS sensor to exhibit an ultrawide detection range (1.27−2783.815 kPa), exceptional sensitivity (up to 21.53 kPa^{-1}), and ultrafast response/recovery times (3.4 ms/34 ms). ALCS can be applied in monitoring

https://doi.org/10.1021/acsami.5c05118
ACS Appl. Mater. Interfaces 2025, 17, 34230−34240

physiological signals, such as head movement, subtle throat vibrations, and muscle pressure during physical activity. Leveraging the remarkable performance of ALCS, the proposed ALCS has been employed in the fabrication of ALCIG. By integrating machine learning algorithms, dynamic sign language recognition and virtual keyboard input recognition have been realized, showcasing the potential of ALCIG as a communication solution for individuals with speech disabilities. In summary, our work highlights the vast application potential of airbag-like comb flexible pressure sensor and their integrated wearable devices in various fields.

■ ASSOCIATED CONTENT

Data Availability Statement

All data are available in the main text or the Supporting Information. The required data can be obtained from the corresponding author or coauthor.

Supporting Information

The Supporting Information is available free of charge at https://pubs.acs.org/doi/10.1021/acsami.5c05118.

Comparison of LDW with Lithography and 3D Printing. (Table S1); Processing diagram of sensing layer. (Figure S1); SEM images of ALCS sensor layer cleaned or not after processing. (Figure S2); material settings for finite element simulation calculation. (Table S2); Simulation comparison between common microstructures. (Figure S3); contact angle test of sensing layer and ALCS (Figure S4); the comparison of the sensitivity and linear pressure range of this work with previous reports. (Table S3); response of ALCS under different microcolumn diameters. (Figure S5); response of ALCS under different pore diameters. (Figure S6); 3D contour plots of ALCS sensing layer processed at different times. (Figure S7); initial/final 100 cycles in cyclic stability test. (Figure S8); detecting changes in subject' different movement states. (Figure S9); detecting changes in subject' different movement states. (Figure S10); physical image of the sensing layer structure between finger joints on ALCIG. (Figure S11); the number and length/width of microstructures placed on ALCIG fingers at various locations. (Table S4); original waveform diagrams of various sign languages collected by ALCIG. (Figure S12); training parameters and evaluation of deep learning models. (Table S5); the meaning represented by each gesture signal. (Table S6) (PDF)

Gesture data collection video (MP4)

■ AUTHOR INFORMATION

Corresponding Author

Xiaohua Wu − *School of Mechanical & Automotive Engineering, South China University of Technology, Guangzhou 510641, China;* orcid.org/0000-0002-0977-0728; Email: mewuxiaohua@mail.scut.edu.cn

Authors

Yingxi Xie − *School of Mechanical & Automotive Engineering, South China University of Technology, Guangzhou 510641, China;* orcid.org/0000-0002-7961-3883

Sheng Bian − *School of Mechanical & Automotive Engineering, South China University of Technology, Guangzhou 510641, China*

Longsheng Lu − *School of Mechanical & Automotive Engineering, South China University of Technology, Guangzhou 510641, China;* orcid.org/0000-0003-3879-4224

Hanxian Chen − *School of Mechanical & Automotive Engineering, South China University of Technology, Guangzhou 510641, China*

Jiayue Liao − *School of Mechanical & Automotive Engineering, South China University of Technology, Guangzhou 510641, China*

Yuxuan Liang − *School of Mechanical & Automotive Engineering, South China University of Technology, Guangzhou 510641, China*

Complete contact information is available at: https://pubs.acs.org/10.1021/acsami.5c05118

Author Contributions

Y.X. and L.L. contributed ideas, supervised the conduct of experiments and the writing of the manuscript. S.B. proposed methods, conducted simulations, completed the design, production, and data analysis of sensors and intelligent gloves, and wrote a manuscript and Supporting Information. H.C. completed the data collection of the sensor. J.L. completed the data collection for the intelligent gloves. Y.L. improved ideas and made revisions to the manuscript. X.W. conceptualized the viewpoint, conducted feasibility verification, implemented machine learning algorithms, and optimized the methods. All the authors discuss the results and refine the manuscript.

Notes

The authors declare no competing financial interest.

■ ACKNOWLEDGMENTS

The current work was financially supported by the National Key Research and Development Project (No. 2020YFB1711300), the National Natural Science Foundation of China (No. 51905178) the Natural Science Foundation of Guangdong Province, China (No. 2021B1515020087) and the Fundamental Research Funds for the Central Universities, SCUT.

■ REFERENCES

(1) Wang, Q.; Li, Y.; Xu, Q.; Yu, H.; Zhang, D.; Zhou, Q.; Dhakal, R.; Li, Y.; Yao, Z. Finger−Coding Intelligent Human−Machine Interaction System Based on All−Fabric Ionic Capacitive Pressure Sensors. *Nano Energy* **2023**, *116*, 108783.

(2) Huangfu, X.; Guo, Y.; Mugo, S. M.; Zhang, Q. Hydrovoltaic Nanogenerators for Self-Powered Sweat Electrolyte Analysis. *Small* **2023**, *19* (15), 2207134.

(3) Liu, S.; Yang, D. S.; Wang, S.; Luan, H.; Sekine, Y.; Model, J. B.; Aranyosi, A. J.; Ghaffari, R.; Rogers, J. A. Soft, Environmentally Degradable Microfluidic Devices for Measurement of Sweat Rate and Total Sweat Loss and for Colorimetric Analysis of Sweat Biomarkers. *EcoMat* **2023**, *5* (1), No. e12270.

(4) Sharma, S.; Thapa, A.; Singh, S.; Mondal, T. Crosstalk-Free Graphene−Liquid Elastomer Based Printed Sensors for Unobtrusive Respiratory Monitoring. *Nanoscale* **2024**, *16* (7), 3498−3509.

(5) Lu, L.; Jiang, C.; Hu, G.; Liu, J.; Yang, B. Flexible Noncontact Sensing for Human−Machine Interaction. *Adv. Mater.* **2021**, *33* (16), 2100218.

(6) Chao, M.; Di, P.; Yuan, Y.; Xu, Y.; Zhang, L.; Wan, P. Flexible Breathable Photothermal-Therapy Epidermic Sensor with MXene for Ultrasensitive Wearable Human-Machine Interaction. *Nano Energy* **2023**, *108*, 108201.

(7) Shi, Y.; Guan, Y.; Liu, M.; Kang, X.; Tian, Y.; Deng, W.; Yu, P.; Ning, C.; Zhou, L.; Fu, R.; Tan, G. Tough, Antifreezing, and Piezoelectric Organohydrogel as a Flexible Wearable Sensor for Human−Machine Interaction. *ACS Nano* **2024**, *18* (4), 3720−3732.
(8) Yin, R.; Wang, D.; Zhao, S.; Lou, Z.; Shen, G. Wearable Sensors-Enabled Human−Machine Interaction Systems: From Design to Application. *Adv. Funct. Mater.* **2021**, *31* (11), 2008936.
(9) Lin, X.; Han, H.; Yang, M.; Yuan, Z.; Chen, Z.; Li, W.-G.; Kang, H.; Zhang, S.; Zhang, Y.; Chen, Y.-X.; Tian, T.; Pang, H. Multicolor Rare-Earth Film with Ultra-Long Afterglow for Diverse Energy-Saving Applications. *Adv. Mater.* **2025**, *37*, 2417420.
(10) Chen, K.; Liu, B.; Hu, N.; Fan, Q.; Zhan, F.; Zhang, Z.; Ni, Z.; Li, X.; Hu, T. A Biodegradable, Highly Sensitive and Multifunctional Mechanical Sensor Based on rGO-Silk Fibroin Hydrogel for Human Motion Detection and Gesture Recognition. *J. Mater. Chem. A* **2024**, *12* (6), 3283−3293.
(11) Wang, L.; Liu, J.; Qi, X.; Liu, H.; Wang, G.; Zhang, X.; Tian, M.; Qu, L. Personal Protective Gloves with Objects Recognizing for Rescuing in Disaster. *Chem. Eng. J.* **2023**, *477*, 146986.
(12) Liu, J.; Wang, L.; Xu, R.; Zhang, X.; Zhao, J.; Liu, H.; Chen, F.; Qu, L.; Tian, M. Underwater Gesture Recognition Meta-Gloves for Marine Immersive Communication. *ACS Nano* **2024**, *18*, 10818.
(13) Bai, N.; Wang, L.; Xue, Y.; Wang, Y.; Hou, X.; Li, G.; Zhang, Y.; Cai, M.; Zhao, L.; Guan, F.; Wei, X.; Guo, C. F. Graded Interlocks for Iontronic Pressure Sensors with High Sensitivity and High Linearity over a Broad Range. *ACS Nano* **2022**, *16* (3), 4338−4347.
(14) Yang, R.; Dutta, A.; Li, B.; Tiwari, N.; Zhang, W.; Niu, Z.; Gao, Y.; Erdely, D.; Xin, X.; Li, T.; Cheng, H. Iontronic Pressure Sensor with High Sensitivity over Ultra-Broad Linear Range Enabled by Laser-Induced Gradient Micro-Pyramids. *Nat. Commun.* **2023**, *14* (1), 1−12.
(15) Lv, C.; Tian, C.; Jiang, J.; Dang, Y.; Liu, Y.; Duan, X.; Li, Q.; Chen, X.; Xie, M. Ultrasensitive Linear Capacitive Pressure Sensor with Wrinkled Microstructures for Tactile Perception. *Adv. Sci.* **2023**, *10* (14), 2206807.
(16) Lai, Q.-T.; Zhao, X.-H.; Sun, Q.-J.; Tang, Z.; Tang, X.-G.; Roy, V. A. L. Emerging MXene-Based Flexible Tactile Sensors for Health Monitoring and Haptic Perception. *Small* **2023**, *19* (27), No. e2300283.
(17) Min, S.; Kim, D. H.; Joe, D. J.; Kim, B. W.; Jung, Y. H.; Lee, J. H.; Lee, B.-Y.; Doh, I.; An, J.; Youn, Y.-N.; Joung, B.; Yoo, C. D.; Ahn, H.-S.; Lee, K. J. Clinical Validation of a Wearable Piezoelectric Blood-Pressure Sensor for Continuous Health Monitoring. *Adv. Mater.* **2023**, *35* (26), 2301627.
(18) Wang, S.; Deng, W.; Yang, T.; Ao, Y.; Zhang, H.; Tian, G.; Deng, L.; Huang, H.; Huang, J.; Lan, B.; Yang, W. Bioinspired MXene-Based Piezoresistive Sensor with Two-Stage Enhancement for Motion Capture. *Adv. Funct. Mater.* **2023**, *33* (18), 2214503.
(19) Wang, Y.; Yue, Y.; Cheng, F.; Cheng, Y.; Ge, B.; Liu, N.; Gao, Y. Ti3C2Tx MXene-Based Flexible Piezoresistive Physical Sensors. *ACS Nano* **2022**, *16* (2), 1734−1758.
(20) Qu, X.; Liu, Z.; Tan, P.; Wang, C.; Liu, Y.; Feng, H.; Luo, D.; Li, Z.; Wang, Z. L. Artificial Tactile Perception Smart Finger for Material Identification Based on Triboelectric Sensing. *Sci. Adv.* **2022**, *8* (31), No. eabq2521.
(21) Wang, X.; Yang, J.; Feng, Z.; Zhang, G.; Qiu, J.; Wu, Y.; Yang, J. Graded Microstructured Flexible Pressure Sensors with High Sensitivity and an Ultrabroad Pressure Range for Epidermal Pulse Monitoring. *ACS Appl. Mater. Interfaces* **2021**, *13* (46), 55747−55755.
(22) Chae, A.; Murali, G.; Lee, S.-Y.; Gwak, J.; Kim, S. J.; Jeong, Y. J.; Kang, H.; Park, S.; Lee, A. S.; Koh, D.-Y.; In, I.; Park, S.-J. Highly Oxidation-Resistant and Self-Healable MXene-Based Hydrogels for Wearable Strain Sensor. *Adv. Funct. Mater.* **2023**, *33*, 2213382.
(23) Miao, J.; Tian, M.; Qu, L.; Zhang, X. Flexible, Transparent and Conductive Wearable Electronic Skin Based on 2D Titanium Carbide (MXene) Ink. *Carbon* **2024**, *222*, 118950.
(24) Jia, B.; Li, Z.; Zheng, T.; Wang, J.; Zhao, Z.-J.; Zhao, L.; Wang, B.; Lu, J.; Zhao, K.; Luo, G.; Li, M.; Lin, Q.; Jiang, Z. Highly-Sensitive, Broad-Range, and Highly-Dynamic MXene Pressure Sensors with Multi-Level Nano-Microstructures for Healthcare and Soft Robots Applications. *Chem. Eng. J.* **2024**, *485*, 149750.
(25) Liang, C.; Sun, J.; Liu, Z.; Tian, G.; Liu, Y.; Zhao, Q.; Yang, D.; Chen, J.; Zhong, B.; Zhu, M.; Xu, H.; Qi, D. Wide Range Strain Distributions on the Electrode for Highly Sensitive Flexible Tactile Sensor with Low Hysteresis. *ACS Appl. Mater. Interfaces* **2023**, *15* (12), 15096−15107.
(26) Li, Y.; Long, J.; Chen, Y.; Huang, Y.; Zhao, N. Crosstalk-Free, High-Resolution Pressure Sensor Arrays Enabled by High-Throughput Laser Manufacturing. *Adv. Mater.* **2022**, *34* (21), 2200517.
(27) Yan, Z.; Wang, L.; Xia, Y.; Qiu, R.; Liu, W.; Wu, M.; Zhu, Y.; Zhu, S.; Jia, C.; Zhu, M.; Cao, R.; Li, Z.; Wang, X. Flexible High-Resolution Triboelectric Sensor Array Based on Patterned Laser-Induced Graphene for Self-Powered Real-Time Tactile Sensing. *Adv. Funct. Mater.* **2021**, *31* (23), 2100709.
(28) Wu, Q.; Qiao, Y.; Guo, R.; Naveed, S.; Hirtz, T.; Li, X.; Fu, Y.; Wei, Y.; Deng, G.; Yang, Y.; Wu, X.; Ren, T.-L. Triode-Mimicking Graphene Pressure Sensor with Positive Resistance Variation for Physiology and Motion Monitoring. *ACS Nano* **2020**, *14* (8), 10104−10114.
(29) Xu, J.; Ma, J.; Peng, Y.; Cao, S.; Zhang, S.; Pang, H. Applications of Metal Nanoparticles/Metal-Organic Frameworks Composites in Sensing Field. *Chin. Chem. Lett.* **2023**, *34* (4), 107527.
(30) Yang, S.; Yang, W.; Yin, R.; Liu, H.; Sun, H.; Pan, C.; Liu, C.; Shen, C. Waterproof Conductive Fiber with Microcracked Synergistic Conductive Layer for High-Performance Tunable Wearable Strain Sensor. *Chem. Eng. J.* **2023**, *453*, 139716.
(31) Yu, Z.; Zhu, Z.; Zhang, Y.; Li, X.; Liu, X.; Qin, Y.; Zheng, Z.; Zhang, L.; He, H. Biodegradable and Flame-Retardant Cellulose-Based Wearable Triboelectric Nanogenerator for Mechanical Energy Harvesting in Firefighting Clothing. *Carbohydr. Polym.* **2024**, *334*, 122040.
(32) Weng, M.; Zhou, J.; Zhou, P.; Shang, R.; You, M.; Shen, G.; Chen, H. Multi-Functional Actuators Made with Biomass-Based Graphene-Polymer Films for Intelligent Gesture Recognition and Multi-Mode Self-Powered Sensing. *Adv. Sci.* **2024**, *11* (22), No. e2309846.
(33) Lee, Y.; Myoung, J.; Cho, S.; Park, J.; Kim, J.; Lee, H.; Lee, Y.; Lee, S.; Baig, C.; Ko, H. Bioinspired Gradient Conductivity and Stiffness for Ultrasensitive Electronic Skins. *ACS Nano* **2021**, *15* (1), 1795−1804.
(34) Lee, G.; Son, J.; Kim, D.; Ko, H. J.; Lee, S. G.; Cho, K. Crocodile-Skin-Inspired Omnidirectionally Stretchable Pressure Sensor. *Small* **2022**, *18* (52), 2205643.
(35) Wu, L.; Li, X.; Choi, J.; Zhao, Z.-J.; Qian, L.; Yu, B.; Park, I. Beetle-Inspired Gradient Slant Structures for Capacitive Pressure Sensor with a Broad Linear Response Range. *Adv. Funct. Mater.* **2024**, *34* (26), 2312370.
(36) Zheng, X.; Chen, L.; Xiao, S.; Meng, Z.; Liu, H.; Wan, G.; He, Y. High-Performance Flexible Pressure Sensor Based on Ordered Double-Level Nanopillar Array Films: Design, Development, and Modeling. *Compos. Sci. Technol.* **2023**, *241*, 110157.
(37) Yao, H.; Sun, T.; Chiam, J. S.; Tan, M.; Ho, K. Y.; Liu, Z.; Tee, B. C. K. Augmented Reality Interfaces Using Virtual Customization of Microstructured Electronic Skin Sensor Sensitivity Performances. *Adv. Funct. Mater.* **2021**, *31* (39), 2008650.
(38) Wang, S.; Zong, Q.; Yang, H.; Tan, C.; Huang, Q.; Liu, X.; Zhang, G.; French, P.; Ye, H. Rapid Fabrication of High-Performance Flexible Pressure Sensors Using Laser Pyrolysis Direct Writing. *ACS Appl. Mater. Interfaces* **2023**, *15* (34), 41055−41066.
(39) Yang, T.; Deng, W.; Chu, X.; Wang, X.; Hu, Y.; Fan, X.; Song, J.; Gao, Y.; Zhang, B.; Tian, G.; Xiong, D.; Zhong, S.; Tang, L.; Hu, Y.; Yang, W. Hierarchically Microstructure-Bioinspired Flexible Piezoresistive Bioelectronics. *ACS Nano* **2021**, *15* (7), 11555−11563.
(40) Du, Q.; Liu, L.; Tang, R.; Ai, J.; Wang, Z.; Fu, Q.; Li, C.; Chen, Y.; Feng, X. High-Performance Flexible Pressure Sensor Based on Controllable Hierarchical Microstructures by Laser Scribing for Wearable Electronics. *Adv. Mater. Technol.* **2021**, *6* (9), 2100122.

https://doi.org/10.1021/acsami.5c05118
ACS Appl. Mater. Interfaces 2025, 17, 34230−34240

(41) Chen, M.; Li, K.; Cheng, G.; He, K.; Li, W.; Zhang, D.; Li, W.; Feng, Y.; Wei, L.; Li, W.; Zhong, G.; Yang, C. Touchpoint-Tailored Ultrasensitive Piezoresistive Pressure Sensors with a Broad Dynamic Response Range and Low Detection Limit. *ACS Appl. Mater. Interfaces* **2019**, *11* (2), 2551−2558.
(42) Li, W.; He, K.; Zhang, D.; Li, N.; Hou, Y.; Cheng, G.; Li, W.; Sui, F.; Dai, Y.; Luo, H.; Feng, Y.; Wei, L.; Li, W.; Zhong, G.; Chen, M.; Yang, C. Flexible and High Performance Piezoresistive Pressure Sensors Based on Hierarchical Flower-Shaped SnSe2 Nanoplates. *ACS Appl. Energy Mater.* **2019**, *2* (4), 2803−2809.
(43) Shin, J.; Ko, J.; Jeong, S.; Won, P.; Lee, Y.; Kim, J.; Hong, S.; Jeon, N. L.; Ko, S. H. Monolithic Digital Patterning of Polydimethylsiloxane with Successive Laser Pyrolysis. *Nat. Mater.* **2021**, *20* (1), 100−107.
(44) Bang, J.; Chun, B.; Lim, J.; Han, Y.; So, H. Ultra-Broad Linear Range and Sensitive Flexible Piezoresistive Sensor Using Reversed Lattice Structure for Wearable Electronics. *ACS Appl. Mater. Interfaces* **2023**, *15* (28), 34120−34131.
(45) Xia, Y.; Whitesides, G. M. Soft Lithography. *Angew. Chem., Int. Ed.* **1998**, *37* (5), 550−575.
(46) Lee, J.; So, H. 3D-Printing-Assisted Flexible Pressure Sensor with a Concentric Circle Pattern and High Sensitivity for Health Monitoring. *Microsyst. Nanoeng.* **2023**, *9* (1), 1−12.
(47) Zhang, C.; Zhou, W.; Geng, D.; Bai, C.; Li, W.; Chen, S.; Luo, T.; Qin, L.; Xie, Y. Laser Direct Writing and Characterizations of Flexible Piezoresistive Sensors with Microstructures. *Opto-Electron. Adv.* **2021**, *4* (4), 200061.
(48) Zhang, C.; Chen, R.; Xiao, C.; Zhao, H.; Wang, Y.; Geng, D.; Chen, S.; Luo, T.; Zhou, W. Laser Direct Writing of Highly Ordered Two-Level Hierarchical Microstructures for Flexible Piezoresistive Sensor with Enhanced Sensitivity. *Adv. Mater. Interfaces* **2022**, *9* (1), 2101596.
(49) Xiao, Y.; Duan, Y.; Li, N.; Wu, L.; Meng, B.; Tan, F.; Lou, Y.; Wang, H.; Zhang, W.; Peng, Z. Multilayer Double-Sided Microstructured Flexible Iontronic Pressure Sensor with a Record-Wide Linear Working Range. *ACS Sens.* **2021**, *6* (5), 1785−1795.
(50) Yuan, H.; Zhang, Q.; Cheng, Y.; Xu, R.; Li, H.; Tian, M.; Ma, J.; Jiao, T. Double-Sided Microstructured Flexible Iontronic Pressure Sensor with Wide Linear Sensing Range. *J. Colloid Interface Sci.* **2024**, *670*, 41−49.
(51) Li, K.; Li, Z.; Wang, W.; Zhang, T.; Yang, X. Design of Double Conductive Layer and Grid-Assistant Face-to-Face Structure for Wide Linear Range, High Sensitivity Flexible Pressure Sensors. *ACS Appl. Mater. Interfaces* **2024**, *16* (11), 14171−14182.
(52) Huang, B.; Feng, J.; He, J.; Huang, W.; Huang, J.; Yang, S.; Duan, W.; Zhou, Z.; Zeng, Z.; Gui, X. High Sensitivity and Wide Linear Range Flexible Piezoresistive Pressure Sensor with Microspheres as Spacers for Pronunciation Recognition. *ACS Appl. Mater. Interfaces* **2024**, *16* (15), 19298−19308.
(53) Huang, F.; Hu, G.; Yu, Z.; Pan, Y.; Yao, H.; Tang, C.; Gu, J.; Zhang, H. Highly Sensitive and Wide Linearity Flexible Pressure Sensor with Randomly Distributed Columnar Arrays. *J. Mater. Sci.* **2023**, *58* (8), 3735−3751.
(54) Chen, Z.; Qu, C.; Yao, J.; Zhang, Y.; Xu, Y. Two-Stage Micropyramids Enhanced Flexible Piezoresistive Sensor for Health Monitoring and Human−Computer Interaction. *ACS Appl. Mater. Interfaces* **2024**, *16* (6), 7640−7649.
(55) Zhong, M.; Zhang, L.; Liu, X.; Zhou, Y.; Zhang, M.; Wang, Y.; Yang, L.; Wei, D. Wide Linear Range and Highly Sensitive Flexible Pressure Sensor Based on Multistage Sensing Process for Health Monitoring and Human-Machine Interfaces. *Chem. Eng. J.* **2021**, *412*, 128649.
(56) Kim, Y.-R.; Kim, M. P.; Park, J.; Lee, Y.; Ghosh, S. K.; Kim, J.; Kang, D.; Ko, H. Binary Spiky/Spherical Nanoparticle Films with Hierarchical Micro/Nanostructures for High-Performance Flexible Pressure Sensors. *ACS Appl. Mater. Interfaces* **2020**, *12* (52), 58403−58411.
(57) Cui, X.; Jiang, Y.; Hu, L.; Cao, M.; Xie, H.; Zhang, X.; Huang, F.; Xu, Z.; Zhu, Y. Synergistically Microstructured Flexible Pressure Sensors with High Sensitivity and Ultrawide Linear Range for Full-Range Human Physiological Monitoring. *Adv. Mater. Technol.* **2023**, *8* (1), 2200609.
(58) Xu, Z.; Wu, D.; Chen, Z.; Wang, Z.; Cao, C.; Shao, X.; Zhou, G.; Zhang, S.; Wang, L.; Sun, D. A Flexible Pressure Sensor with Highly Customizable Sensitivity and Linearity via Positive Design of Microhierarchical Structures with a Hyperelastic Model. *Microsyst. Nanoeng.* **2023**, *9* (1), 1−12.
(59) Lu, C.; Gao, Y.; Chan, X.; Yu, W.; Wang, H.; Hu, L.; Li, L. A Cross-Scale Honeycomb Architecture-Based Flexible Piezoresistive Sensor for Multiscale Pressure Perception and Fine-Grained Identification. *Mater. Horiz.* **2024**, *11* (2), 510−518.

https://doi.org/10.1021/acsami.5c05118
ACS Appl. Mater. Interfaces 2025, 17, 34230−34240